APPLIED PHYSICS

# Self-aligned patterning technique for fabricating high-performance diamond sensor arrays with nanoscale precision

**Mengqi Wang[1,2], Haoyu Sun[1,2], Xiangyu Ye[1,2], Pei Yu[1,2], Hangyu Liu[1,2], Jingwei Zhou[1,2], Pengfei Wang[1,2,3], Fazhan Shi[1,2,3], Ya Wang[1,2,3]*, Jiangfeng Du[1,2,3]***



**Efficient, nanoscale precision alignment of defect center creation in photonics structures in challenges the realization of high-performance photonic devices and quantum technology applications. Here, we propose a facile self-aligned patterning technique based on conventional engineering technology, with doping precision that can reach ~15 nm. We demonstrate this technique by fabricating diamond nanopillar sensor arrays with high consistency and near-optimal photon counts. The sensor array achieves high yield approaching the theoretical limit, and high efficiency for filtering sensors with different numbers of nitrogen vacancy centers. Combined with appropriate crystal orientation, the system achieves a saturated fluorescence rate of 4.34 Mcps and effective fluorescence-dependent detection sensitivity of 1800 $cps^{-1/2}$. These sensors also show enhanced spin properties in the isotope-enriched diamond. Our technique is applicable to all similar solid-state systems and could facilitate the development of parallel quantum sensing and scalable information processing.**

## INTRODUCTION

Arranging artificial atom qubits in a diamond to formulate spin arrays with long coherence times (*1*) and efficient spin-photon interface (*2*) is attractive for parallel quantum sensing and scalable information processing. To improve the diamond-based quantum technique for practical applications, enthusiastic efforts are devoted in the past few years to develop diamond nanostructures for enhancing the photon collection efficiency, such as solid immersion lenses [~1 mega counts per second (Mcps)] (*3*–*5*), pillar-shaped waveguide (~1.7 Mcps) (*6*, *7*), circular bullseye grating (~2.7 Mcps) (*8*), parabolic reflector (~4 Mcps) (*9*), and inverted nanocones (~2.7 Mcps) (*10*). These photonic structures can theoretically raise the fluorescence collection efficiency from 5 to 30 to 80%. Although individual spin qubits integrated with photonic structures (*3*–*16*) can now achieve excellent performance including functional quantum repeater nodes (*17*–*19*) and nanoscale magnetic field sensors (*20*–*22*), placing emitters into the optimal position of the individual photonic nanostructures remains an outstanding challenge (*23*). In addition to achieving nanoscale doping (*24*–*26*), the alignment of doping to the photonic structure also requires nanoscale precision, which is challenging and a critical barrier to large-scale quantum information processing with diamond qubits.

Enthusiastic efforts are thus devoted in the past few years to achieving the above goal by combining and aligning two independent fabrication systems of the diamond doping and photonic structure etching, respectively. One conventional strategy is to fabricate the photonic structure at the prelocated position of color centers determined by optical fluorescence imaging (*9*). Because of the randomness of color centers, the alignment process of this method is complex and inefficient. Substantially, the engineering of large-scale photonic device arrays is challenging to achieve using this strategy. Another one is to implant target ions into photonic structures prepared in advance. It thus requires a specially designed implantation system like atomic force microscope–assisted ion implantation (*26*–*28*) and focused ion beam implantation (*29*–*34*). The implantation precision is limited by the size of the mask hole or the ion beam spot, and the alignment accuracy is determined by how precisely the structure is imaged. The reported prelocated or implantation precision and alignment accuracy are 20 to 30 nm (*9*, *33*, *35*). A promising alternative strategy to alleviate these constraints is self-aligned patterning, which combines the independent processes through a single pattern to eliminate the aligned inaccuracy. At the same time, it greatly simplifies the design and fabrication process. Therefore, the self-aligned pattern process has been widely implicated in the semiconductor chip manufacturing. Recently, preliminary demonstrations of this strategy in diamond nanofabrication have been implemented (*36*, *37*), but the manual high-precision hard mask transfer process (*38*) is required, limiting its scalability. The expected advantage of self-alignment in making high-performance diamond devices is not yet demonstrated.

Here, we introduce a facile self-aligned patterning technique wholly based on conventional engineering technology, and the doping precision of ~15 nm is achieved. It can be applied to the fabrication of various photonic structures like nanopillar, parabolic reflector, planar waveguide, ring resonator, etc. Specifically, we demonstrate this technique by fabricating diamond nanopillar sensors (*6*, *7*, *39*), which are widely used in nanoscale magnetic resonance spectroscopy (*40*) and scanning imaging (*41*–*46*). The self-aligned sensor arrays show high consistency and near-optimal photon counts, high yield approaching the theoretical limit, and high efficiency for filtering sensors with different numbers of nitrogen vacancy (NV) centers. We further controlled the emission dipole orientation through the diamond crystal orientation, achieving a saturated fluorescence rate of 4.34 Mcps and the best reported fluorescence-dependent detection sensitivity.

[1]CAS Key Laboratory of Microscale Magnetic Resonance and School of Physical Sciences, University of Science and Technology of China, Hefei 230026, China. [2]CAS Center for Excellence in Quantum Information and Quantum Physics, University of Science and Technology of China, Hefei 230026, China. [3]Hefei National Laboratory, University of Science and Technology of China, Hefei 230088, China.
*Corresponding author. Email: ywustc@ustc.edu.cn (Y.W.); djf@ustc.edu.cn (J.D.)

## RESULTS

### The fabrication process based on self-aligned patterning

Figure 1A shows the diamond nanopillar sensor with a single NV center embedded in it. Figure 1B shows the simulated dependence of collection efficiency in both longitudinal and lateral directions. For a typical top diameter of 380 nm, one can find that the structure approaches its optimal performance for NV centers inside the lateral central areas of 40-nm radius and near diamond surface (<20 nm) in the longitudinal direction. The traditional fabrication method adopts a top-down processing without alignment (Fig. 1C). The resulting distribution of NV centers inside the structure is random. In comparison, the self-aligned technique controls both the diamond doping and the fabrication by a well-designed double-layer mask (Fig. 1D). The top polymethyl methacrylate (PMMA) pattern acts as both a diamond doping mask to constrain the ion implantation region and a wet etching mask for isotropic wet etching of the polydimethylglutarimide (PMGI) pattern. The bottom PMGI pattern constrains the self-alignment between the ion implantation region and the center of the resist.

Figure 2A describes the whole process of self-alignment in detail. The lateral straggling of ion in diamond caused by implantation can be ignored (about 2 nm at 5 keV) (*47*). Therefore, the implantation precision depends entirely on the size of the PMMA mask. As shown in Fig. 2 (B and C), the ion implantation precision can achieve to about 15 nm, which is characterized by an electron beam evaporation process (see the Supplementary Materials for details). In addition, higher precision can be further obtained by depositing on the PMMA mask hole's sidewall (*24*, *25*). Conical cylinders arrays shown in Fig. 2 (E and F) are fabricated through a trifluoromethane ($CHF_3$) and $O_2$ mixed gas etching process, which is also suitable for fabricating a cylinder (*6*, *48*) and a parabolic reflector (*49*). In addition, inverted nanocones can be obtained by introducing Faraday cage–assisted etching into the process (*10*). In addition to the devices based on circular resist etching, the self-aligned patterning technique can also be applied to optimize the device-coupled single emitter to other micro-/nanostructures, such as the planar optical waveguide, ring resonator, bullseye grating, etc. (*8*, *11*, *50*), which can be fabricated by changing the PMMA layer pattern to line, ring, concentric ring, etc.

### Performance of self-aligned sensors

To characterize the self-aligned technique, we first compare the NV sensors' performance with the same conical cylinder's shape, fabricated

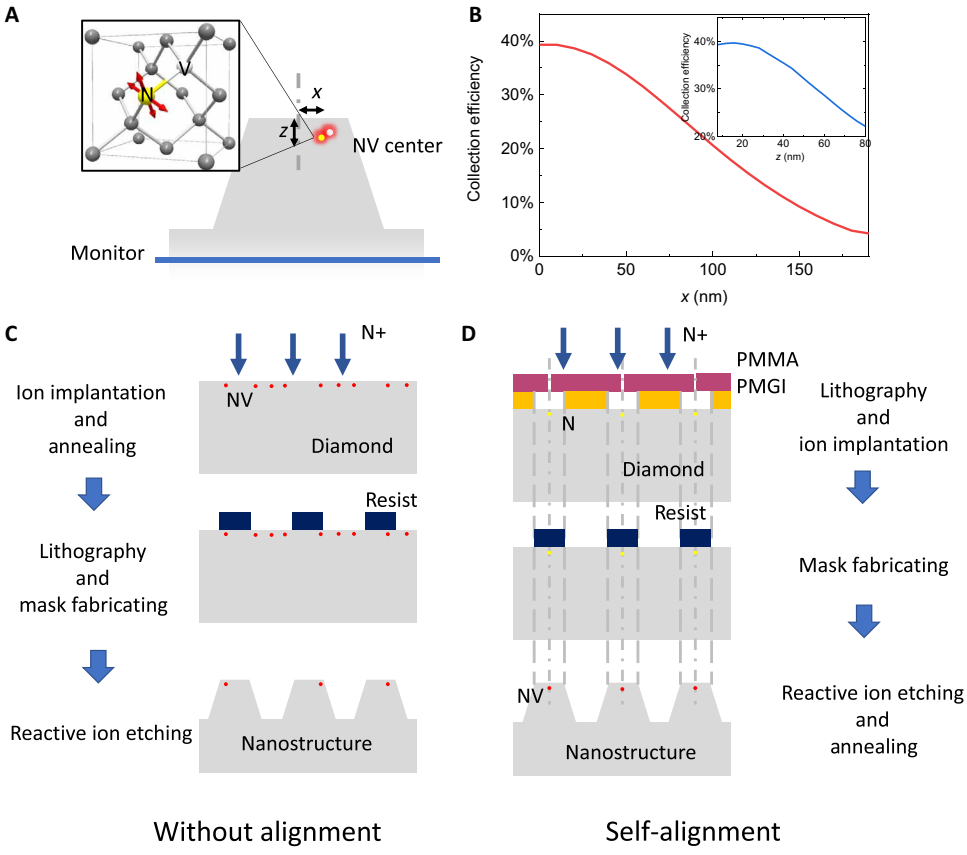


**Fig. 1. The conceptual demonstration of the difference of fabricating diamond nanopillar sensors with or without self-aligned technique.** (**A**) The finite-difference time-domain (FDTD) simulation model (see Materials and Methods). (**B**) The simulation results illustrating the importance of precise localization of NV centers into nanopillar sensors. The collection efficiency [numerical aperture (NA) = 0.7] as a function of $x$ ($z$ = 8 nm). The inset shows the collection efficiency as a function of $z$ ($x$ = 0). (**C**) Illustration of the fabrication process of photonic structures based on a top-down method without alignment. The NV center is generated by maskless ion implantation and annealing. The resist is prepared by photolithography or electron beam lithography, and the photonic structure is formed by reactive plasma etching. (**D**) Illustration of the fabrication process of photonic structures based on self-alignment. PMGI + PMMA double layer on the diamond is used to constrain the position of the etching mask and ion implantation region.

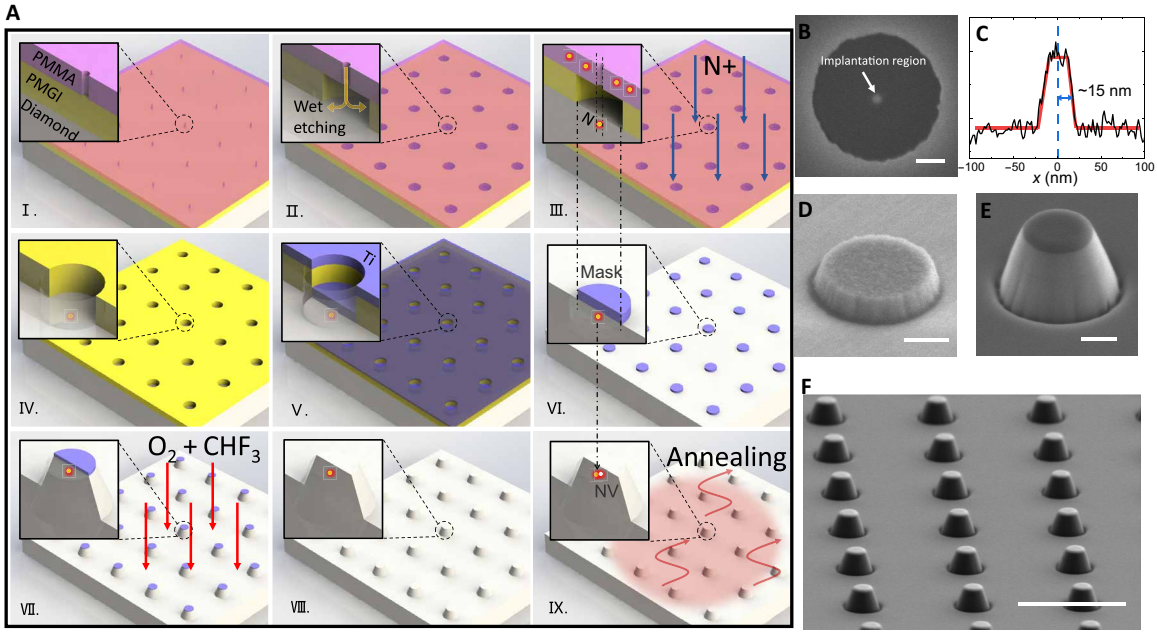


**Fig. 2. The fabrication process to realize self-aligned patterning and based sensor arrays.** (**A**) Schematic of fabrication steps. (I) Spin-coating PMGI ~270-nm (yellow) and PMMA ~210-nm (pink) double layers on diamond and making holes array in the PMMA layer by electron beam lithography. (II) Isotropic wet etching of PMGI layer with 2.38% tetramethylammonium hydroxide (TMAH). (III) Doping nitrogen into diamond by ion implantation through hole array in PMMA layer. (IV) Removing the PMMA layer with acetone. (V) Coating titanium of ~100 nm (blue) by electron beam evaporation (VI) liftoff processing in *N*-methyl pyrrolidone. (VII) Forming conical cylinder by $CHF_3 + O_2$ reactive ion etching ($CHF_3$:$O_2$, 5:30 standard cubic centimeters per minute). (VIII) Removing the Ti layer with a buffered oxide etch. (IX) Converting nitrogen to NV center by annealing at 1000°C. (**B**) Verification of ion implanted region in (III) by metal deposition and scanning electron microscopy (SEM) characterization (scale bar, 100 nm). The metal position in the center of the image represents the ion implantation region (see the Supplementary Materials for details). (**C**) SEM imaging contrast shows that the radius of ion implantation region is ~15 nm. (**D**) SEM image of a metal Ti mask in VI (scale bar, 200 nm). (**E**) SEM image of a conical cylinder by $CHF_3 + O_2$ reactive ion etching in VII (scale bar, 200 nm). (**F**) SEM image of an array of conical cylinders (scale bar, 2 μm).

with and without self-alignment using a (100)-oriented diamond with natural isotopic abundances. The radius of the self-aligned ion implantation mask is set at 40 nm. A total of 207 self-aligned sensors and 215 nonaligned sensors are investigated for the fluorescence intensity statics. As shown in Fig. 3 (C and D), the nonaligned sensors show greatly varied photon counts due to randomly distributed NV centers, while the self-aligned sensors have high consistency and near-optimal photon counts. In addition, it should be cautious about the actual number of NV centers and the corresponding photon counts due to the inconsistency in these nonaligned sensors. The second-order photon correlation measurement further verifies this. As shown in Fig. 3A, for nonaligned sensors with similar photon counts of about 1.7 and 1.8 Mcps, $g^{(2)}(0)$ shows distinct values, indicating that sensors with the same photon counts may have different NV numbers [$g^{(2)}(0)$~0.03 for single NV centers and $g^{(2)}(0)$~0.56 for double NV centers]. In addition, for nonaligned sensors with photon counts of about 2.2 Mcps, the values of $g^{(2)}(0)$ show between 0 and 0.5 and may contain two or more single-photon sources with different brightness. Therefore, the criterion of the single-photon source [$g^{(2)}(0) < 0.5$] is no longer applicable for the nonaligned sensors. A more complicated process like performing optically detected magnetic resonance in a gradient magnetic field is required for safe judgment (*51*). In contrast, self-aligned sensors show high consistency, enabling the direct determination of the number of NV centers by photon counts. In this case, the measured photon antibunching obeys the standard criterion [$g^{(2)}(0) = 0.096(6)$ for a single NV center of 1.7 Mcps, $g^{(2)}(0) = 0.522(3)$ for double NV centers of 2.8 Mcps, and $g^{(2)}(0) = 0.804(2)$ for four NV centers of 6.1 Mcps]. In Fig. 3G, we count the number of NV centers in the aligned sensors according to the photon counts. The probability displays the expected Poisson distribution due to ion implantation, further showing this high consistency. The proportion of single NV sensors has reached 33.4% ($\lambda = 0.7$), close to the limit of 36.8% ($\lambda = 1$) under the optimal implantation dose condition. The $T_2$, $T_2$*, and $T_1$ coherence times of NV centers are also estimated by randomly measuring the NV centers in the same direction. The statistical results (Fig. 3, E to G) show a similar coherence time distribution in both sensors. Further combing the isotope-enriched, (100)-oriented diamond ($^{12}C$ 99.999%), the devices achieve high photon counts and enhanced the coherence time (inset in Fig. 3, D to F).

As another critical requirement, dipole direction control should be considered to achieve optimal performance devices. Because NV centers have deterministic [111] direction in the diamond lattice, we show this dipole direction control by adjusting the single-crystal diamond orientation. According to our finite-difference time-domain (FDTD) simulation (Fig. 4B), the (111)-oriented single crystal diamond, with one-fourth of NV centers perpendicular to the diamond surface, will have the best performance in collection efficiency. The corresponding experimental measurements are summarized in Fig. 4A. Benefiting from the self-aligned technique, the average saturated photon counts of NV centers are improved to 3.7 ± 0.6 Mcps [with a numerical aperture (NA) = 1.42 oil-immersion objective] and 2.6 ± 0.4 Mcps (measured with an NA = 0.7 air/dry objective). The photon counts of different directions obey the theoretical simulation

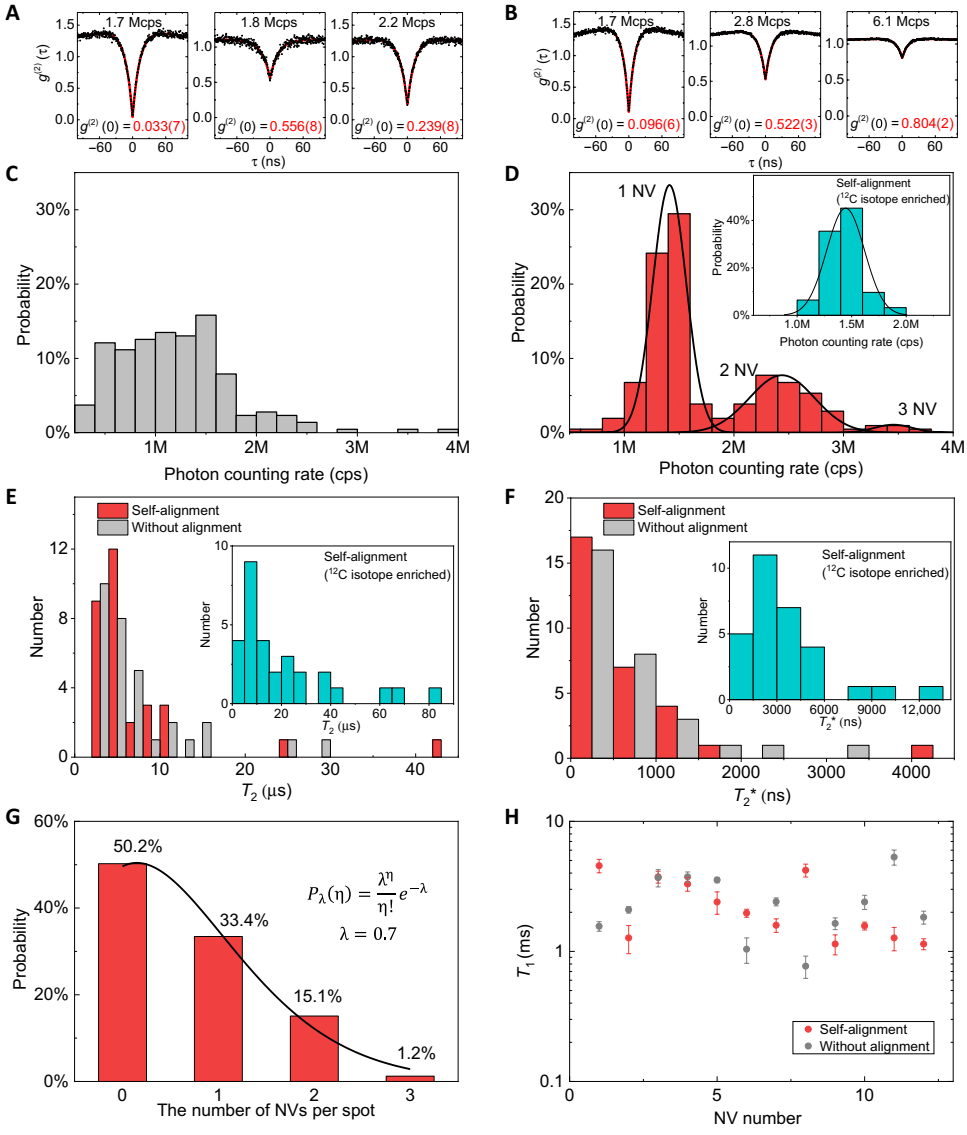


**Fig. 3. Comparison of the self-aligned sensors and nonaligned sensors prepared on a (100)-oriented diamond.** (**A**) The second-order correlation function $g^{(2)}(\tau)$ (measured at an excitation power of ~40 μW) of the nonaligned devices with different photon counting rates. (**B**) The second-order correlation function $g^{(2)}(\tau)$ (measured at an excitation power of ~40 μW) of the self-aligned devices with different photon counting rates. (**C**) Distribution of photon counting rate of NV sensors without alignment (at an excitation power of ~800 μW). (**D**) Distribution of photon counting rate of NV sensors by self-aligned (at an excitation power of ~800 μW). The black line is the Gaussian fitting to the data envelope, and the number of NV centers in the photonic device can be distinguished by the envelope. The inset shows the distribution of photon counting rate of a single NV sensor by self-aligned in an isotope-enriched diamond ($^{12}$C 99.999%). (**E** and **F**) Histogram of the $T_2$ (Hahn echo pulse sequence) and $T_2$*coherence time. The red and gray bars show the NV center sensors fabricated by self-alignment and without alignment, respectively. In addition, the inset shows the sensors fabricated by self-alignment in an isotope-enriched diamond ($^{12}$C 99.999%) (**G**) The distribution of the number of NV in self-aligned devices obtained from (D) and fitted to a Poisson distribution. (**H**) The $T_1$ coherence time measurement. The red and gray points show the NV center sensors fabricated by self-alignment and without alignment, respectively.

(Fig. 4B). The saturation fluorescence rate of the NV center shown in Fig. 4C has reached 4.34 ± 0.03 Mcps.

The shot-noise–limited magnetic field sensitivity of the single NV center is mainly determined by a photon counting rate and spin coherence time of the NV center, which can be expressed as (*52*)

$$\delta B \propto \frac{\hbar}{g_e \mu_B} \frac{1}{R\sqrt{S}} \frac{1}{\sqrt{T_{spin}}}$$

where $\hbar$ is the reduced Planck constant, $g_e \approx 2.003$ is the NV electronic $g$ factor, $\mu_B$ is the Bohr magneton, $R \approx 30\%$ is the optically detected magnetic resonance (ODMR) contrast of NV center (see fig. S6 for ODMR contrast measurements of the devices), and $S$ is the photon counting rate of NV center. $T_{spin}$ is the coherence time of the NV center (for ac magnetic field detection, $T_{spin} \sim T_2$, and for DC magnetic field detection, $T_{spin} \sim T_2^*$).

Because the background photons account for the reduction of NV sensors' magnetic sensitivity, the shot-noise part is corrected as

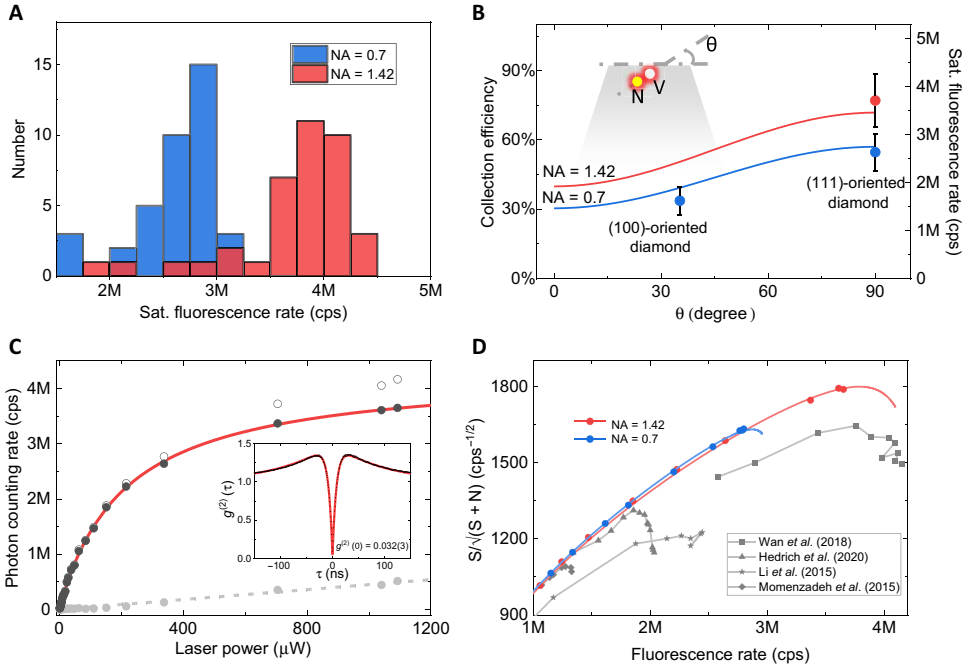


**Fig. 4. Performance of the nanopillar sensor arrays with direction control.** (**A**) Histogram of the saturation fluorescence rate (background subtracted) of NV centers. The blue and red bars indicate the data measured with an NA = 0.7 air/dry objective and an NA = 1.42 oil-immersion objective, respectively. (**B**) Comparison of the simulated and experimental results for different θ (the angle between NV axis and diamond surface) with an NA = 0.7 air/dry objective (blue) and an NA = 1.42 oil-immersion objective (red). The solid line corresponding to the left axis is the result of simulation. The point corresponding to the right axis is the statistical mean of the experimental results, and the error bar is the statistical SD. (**C**) Laser power–dependent fluorescence count rate measurements for one of the NV centers in (A) by NA = 1.42 oil-immersion objective. The hollow black circles are the photon counting rate data. The bold gray circles are the background count rate data obtained from the value of $g^{(2)}(0)$, and the gray dashed line is a linear fitting for the background. The bold black circles are the background-subtracted fluorescence rates. The red line is the fitted saturation curve, and the saturation fluorescence rate is 4.34 ± 0.03 Mcps. The inset shows the $g^{(2)}(\tau)$ (measured at an excitation power of ~40 μW). (**D**) Fluorescence rate as a function of fluorescence-dependent detection sensitivity. Our results are expressed in red (measured with an NA = 1.42 oil-immersion objective) and blue (measured with an NA = 0.7 air/dry objective objective), where the bold circle and solid line are obtained from the experimental data and saturation curve, respectively. The experimental results of NV center photonic structures reported are marked as a reference (*7*–*9*, *49*).

$$\frac{1}{\sqrt{S}} \rightarrow 1/\frac{S}{\sqrt{S+N}}$$

where $S$ is the fluorescence count rate of NV center and $N$ is the background count rate.

Figure 4D and table S1 (in the Supplementary Materials) first compares the shot-noise between the self-aligned sensors and previously reported sensors. Because of the high photon counts and a low background, self-aligned sensors show the most heightened fluorescence-dependent detection sensitivity ($S/\sqrt{S+N}$) of ~1800 cps$^{-1/2}$. Compared with the case without nanostructures ($S$ ~200 kcps, ~450 cps$^{-1/2}$), the detection sensitivity is improved by about four times. For the spin coherence part, as shown in Fig. 3, the self-aligned sensors in isotope-enriched diamond show enhanced coherence time ($T_2$ and $T_2$* are both increased by about three to five times on average), corresponding to about two times enhancement of detection sensitivity. Further enhancement could be achieved by combining with the diamond surface engineering (*53*) or multipulse dynamical decoupling methods (*54*, *55*).

## DISCUSSION

In summary, we propose a facile self-aligned patterning technique and demonstrate its power in fabricating high-performance diamond nanopillar sensors. The ~15-nm doping precision achieved is sufficient for fabricating other high-quality, position-sensitive emitter-photonic structures such as planar waveguides and ring resonators. The demonstrated precision can be further improved by sidewall deposition (*24*, *25*). Although the bottom double-layer masks are patterned by isotropic wet etching in this work, they can also be patterned directly by electron beam lithography (*56*), which would be suitable for complex patterning applications. For more refined fabrication, the multilayer masks could be used to construct the undercut structure in the liftoff process. In addition, introducing techniques such as quasi-isotropic etching (*57*, *58*), angular etching (*59*), and sidewall polishing would help fabricate complex high-quality diamond photonics cavities.

For high-performance sensor arrays fabrication, this technique is fully compatible with other diamond fabrication processes, like diamond surface treatment (*53*), high-temperature annealing (*60*, *61*), lattice charging (*62*), and n-type diamond (*63*–*65*), to further improve the creation yield and spin and optical properties of color centers in devices. The self-aligned patterning technique demonstrated here for NV centers could be extended to other similar solid-state systems such as silicon carbide, rare-earth ions, etc. In addition, this technique should facilitate the development of parallel quantum sensing and scalable information processing.

## MATERIALS AND METHODS

### FDTD simulation

The FDTD simulation (Lumerical Solutions Ltd.) is used to numerically calculate the collection efficiency of the nanopillar used in experiment. The emission of fluorescence is associated with two orthogonal dipoles located in a plane perpendicular to the NV symmetry axis, which are marked by the red vectors in the inset of Fig. 1A (*5*, *66*). In FDTD simulation, we take two incoherence electric dipoles ($\lambda$ = 637 nm) that are orthogonal to each other and perpendicular to the NV axis to simulate the fluorescence emission of the NV center. The nanopillar model follows the actual structure, which was acquired through the scanning electron microscope: height, ~350 nm; top diameter, ~380 nm; and angle between sidewall and plane, ~69° (see fig. S4 for the effect of geometry on collection efficiency). As shown in Fig. 1A, the monitor was set below the nanopillar structure to get the dipole emission far-field projection. In addition, the far-field projection is recalculated on the basis of Snell's law and the Fresnel equations to consider the reflection and refraction on the interface. In analyzing the results, the collection efficiency can be expressed as

$$\eta = I_{NA}/I_{source}$$

where $I_{NA}$ is the integration of the far-field electric field intensity within the objective collection angle and $I_{source}$ is the source power emitted in bulk diamond.

### Device fabrication

The diamond used in the experiment consisted of a 50-μm-thick, (100)-oriented chemical vapor deposition and a (111)-oriented high-pressure high-temperature (HPHT) single-crystal diamond. In addition, both are polished to a Ra of <3 nm. The diamond was first cleaned in a boiling 1:1:1 nitric, perchloric, and sulfuric acid bath to remove surface contamination.

For the sensors array with self-align strategy (shown in Fig. 2), a PMGI layer with the thickness of ~270 nm and a PMMA layer with the thickness of ~210 nm were spin-coated on a diamond, and hole arrays were fabricated on the PMMA by 100 keV electron beam lithography. The isotropic wet etching of PMGI pattern was carried out by 2.38% tetramethylammonium hydroxide (TMAH) through holes in PMMA. Hole arrays in PMMA are used as ion implantation mask to dope ions into the center of PMGI pattern, and, according to the simulation, the nitrogen ions with an energy of <20 keV would fully stopped by the 210-nm thickness of the PMMA layer (*47*). After ion implantation, the PMMA layer was removed by acetone and washed with isopropanol and then dried by nitrogen. The pattern on PMGI is transferred to Ti masks by an electron beam evaporation of 100-nm Ti and a liftoff process in *N*-methyl pyrrolidone. After that, the inductively coupled plasma, reactive ion etching system is used to etch the conical cylinder photonic structures, with $CHF_3$:$O_2$ 5:30–standard cubic centimeter per minute mixed gas. After buffered oxide etching of the residual Ti, the nitrogen is converted to NV center by annealing at 1000°C in vacuum. The sample with natural isotopic abundances used the hole arrays with a radius of 40 nm and implanted with atomic nitrogen at an energy of 5 keV and a dose of $5 \times 10^{11}$ $cm^{-2}$. In addition, the sample with isotope enrichment ($^{12}C$ 99.999%) used the hole arrays with a radius of 15 nm and implanted with atomic nitrogen at an energy of 15 keV and a dose of $1 \times 10^{12}$ $cm^{-2}$.

For the sensors array without alignment, the maskless ion implantation is used with atomic nitrogen at an energy of 5 keV and a dose of $6 \times 10^{10}$ $cm^{-2}$, and the nitrogen is converted to the NV center by annealing in 1000°C in vacuum. The Ti masks is directly made by an electron beam lithography and liftoff process, and the same diamond etching process as self-aligning sensor is used. Before the test, all of the sensors are cleaned in an additional acid bath and annealed at 580°C in air for 20 min.

## SUPPLEMENTARY MATERIALS

Supplementary material for this article is available at https://science.org/doi/10.1126/sciadv.abn9573

## REFERENCES AND NOTES


1. C. E. Bradley, J. Randall, M. H. Abobeih, R. C. Berrevoets, M. J. Degen, M. A. Bakker, M. Markham, D. J. Twitchen, T. H. Taminiau, A ten-qubit solid-state spin register with quantum memory up to one minute. *Phys. Rev. X* **9**, 031045 (2019).
2. D. D. Awschalom, R. Hanson, J. Wrachtrup, B. B. Zhou, Quantum technologies with optically interfaced solid-state spins. *Nat. Photonics* **12**, 516–527 (2018).
3. L. Marseglia, J. P. Hadden, A. C. Stanley-Clarke, J. P. Harrison, B. Patton, Y. L. D. Ho, B. Naydenov, F. Jelezko, J. Meijer, P. R. Dolan, J. M. Smith, J. G. Rarity, J. L. O'Brien, Nanofabricated solid immersion lenses registered to single emitters in diamond. *Appl. Phys. Lett.* **98**, 133107 (2011).
4. M. Jamali, I. Gerhardt, M. Rezai, K. Frenner, H. Fedder, J. Wrachtrup, Microscopic diamond solid-immersion-lenses fabricated around single defect centers by focused ion beam milling. *Rev. Sci. Instrum.* **85**, 123703 (2014).
5. P. Siyushev, F. Kaiser, V. Jacques, I. Gerhardt, S. Bischof, H. Fedder, J. Dodson, M. Markham, D. Twitchen, F. Jelezko, J. Wrachtrup, Monolithic diamond optics for single photon detection. *Appl. Phys. Lett.* **97**, 241902 (2010).
6. T. M. Babinec, B. J. Hausmann, M. Khan, Y. Zhang, J. R. Maze, P. R. Hemmer, M. Loncar, A diamond nanowire single-photon source. *Nat. Nanotechnol.* **5**, 195–199 (2010).
7. S. A. Momenzadeh, R. J. Stohr, F. F. de Oliveira, A. Brunner, A. Denisenko, S. Yang, F. Reinhard, J. Wrachtrup, Nanoengineered diamond waveguide as a robust bright platform for nanomagnetometry using shallow nitrogen vacancy centers. *Nano Lett.* **15**, 165–169 (2015).
8. L. Li, E. H. Chen, J. Zheng, S. L. Mouradian, F. Dolde, T. Schroder, S. Karaveli, M. L. Markham, D. J. Twitchen, D. Englund, Efficient photon collection from a nitrogen vacancy center in a circular bullseye grating. *Nano Lett.* **15**, 1493–1497 (2015).
9. N. H. Wan, B. J. Shields, D. Kim, S. Mouradian, B. Lienhard, M. Walsh, H. Bakhru, T. Schroder, D. Englund, Efficient extraction of light from a nitrogen-vacancy center in a diamond parabolic reflector. *Nano Lett.* **18**, 2787–2793 (2018).
10. S. W. Jeon, J. Lee, H. Jung, S. W. Han, Y. W. Cho, Y. S. Kim, H. T. Lim, Y. Kim, M. Niethammer, W. C. Lim, J. Song, S. Onoda, T. Ohshima, R. Reuter, A. Denisenko, J. Wrachtrup, S. Y. Lee, Bright nitrogen-vacancy centers in diamond inverted nanocones. *Acs Photonics* **7**, 2739–2747 (2020).
11. B. J. Hausmann, B. Shields, Q. Quan, P. Maletinsky, M. McCutcheon, J. T. Choy, T. M. Babinec, A. Kubanek, A. Yacoby, M. D. Lukin, M. Lončar, Integrated diamond networks for quantum nanophotonics. *Nano Lett.* **12**, 1578–1582 (2012).
12. A. Faraon, C. Santori, Z. Huang, V. M. Acosta, R. G. Beausoleil, Coupling of nitrogen-vacancy centers to photonic crystal cavities in monocrystalline diamond. *Phys. Rev. Lett.* **109**, 033604 (2012).
13. A. Faraon, P. E. Barclay, C. Santori, K. M. C. Fu, R. G. Beausoleil, Resonant enhancement of the zero-phonon emission from a colour centre in a diamond cavity. *Nat. Photonics* **5**, 301–305 (2011).
14. L. Li, T. Schroder, E. H. Chen, M. Walsh, I. Bayn, J. Goldstein, O. Gaathon, M. E. Trusheim, M. Lu, J. Mower, M. Cotlet, M. L. Markham, D. J. Twitchen, D. Englund, Coherent spin control of a nanocavity-enhanced qubit in diamond. *Nat. Commun.* **6**, 6173 (2015).
15. C. T. Nguyen, D. D. Sukachev, M. K. Bhaskar, B. Machielse, D. S. Levonian, E. N. Knall, P. Stroganov, C. Chia, M. J. Burek, R. Riedinger, H. Park, M. Loncar, M. D. Lukin, An integrated nanophotonic quantum register based on silicon-vacancy spins in diamond. *Phys. Rev. B* **100**, 165428 (2019).
16. N. H. Wan, T. J. Lu, K. C. Chen, M. P. Walsh, M. E. Trusheim, L. De Santis, E. A. Bersin, I. B. Harris, S. L. Mouradian, I. R. Christen, E. S. Bielejec, D. Englund, Large-scale integration of artificial atoms in hybrid photonic circuits. *Nature* **583**, 226–231 (2020).
17. W. Pfaff, B. J. Hensen, H. Bernien, S. B. van Dam, M. S. Blok, T. H. Taminiau, M. J. Tiggelman, R. N. Schouten, M. Markham, D. J. Twitchen, R. Hanson, Quantum information. Unconditional quantum teleportation between distant solid-state quantum bits. *Science* **345**, 532–535 (2014).
18. P. C. Humphreys, N. Kalb, J. P. J. Morits, R. N. Schouten, R. F. L. Vermeulen, D. J. Twitchen, M. Markham, R. Hanson, Deterministic delivery of remote entanglement on a quantum network. *Nature* **558**, 268–273 (2018).

19. N. Kalb, A. A. Reiserer, P. C. Humphreys, J. J. W. Bakermans, S. J. Kamerling, N. H. Nickerson, S. C. Benjamin, D. J. Twitchen, M. Markham, R. Hanson, Entanglement distillation between solid-state quantum network nodes. *Science* **356**, 928–932 (2017).
20. J. R. Maze, P. L. Stanwix, J. S. Hodges, S. Hong, J. M. Taylor, P. Cappellaro, L. Jiang, M. V. Dutt, E. Togan, A. S. Zibrov, A. Yacoby, R. L. Walsworth, M. D. Lukin, Nanoscale magnetic sensing with an individual electronic spin in diamond. *Nature* **455**, 644–647 (2008).
21. G. Balasubramanian, I. Y. Chan, R. Kolesov, M. Al-Hmoud, J. Tisler, C. Shin, C. Kim, A. Wojcik, P. R. Hemmer, A. Krueger, T. Hanke, A. Leitenstorfer, R. Bratschitsch, F. Jelezko, J. Wrachtrup, Nanoscale imaging magnetometry with diamond spins under ambient conditions. *Nature* **455**, 648–651 (2008).
22. J. M. Taylor, P. Cappellaro, L. Childress, L. Jiang, D. Budker, P. R. Hemmer, A. Yacoby, R. Walsworth, M. D. Lukin, High-sensitivity diamond magnetometer with nanoscale resolution. *Nat. Phys.* **4**, 810–816 (2008).
23. P. Senellart, G. Solomon, A. White, High-performance semiconductor quantum-dot single-photon sources. *Nat. Nanotechnol.* **12**, 1026–1039 (2017).
24. D. Scarabelli, M. Trusheim, O. Gaathon, D. Englund, S. J. Wind, Nanoscale engineering of closely-spaced electronic spins in diamond. *Nano Lett.* **16**, 4982–4990 (2016).
25. I. Bayn, E. H. Chen, M. E. Trusheim, L. Li, T. Schroder, O. Gaathon, M. Lu, A. Stein, M. Liu, K. Kisslinger, H. Clevenson, D. Englund, Generation of ensembles of individually resolvable nitrogen vacancies using nanometer-scale apertures in ultrahigh-aspect ratio planar implantation masks. *Nano Lett.* **15**, 1751–1758 (2015).
26. S. Pezzagna, D. Wildanger, P. Mazarov, A. D. Wieck, Y. Sarov, I. Rangelow, B. Naydenov, F. Jelezko, S. W. Hell, J. Meijer, Nanoscale engineering and optical addressing of single spins in diamond. *Small* **6**, 2117–2121 (2010).
27. S. Pezzagna, D. Rogalla, D. Wildanger, J. Meijer, A. Zaitsev, Creation and nature of optical centres in diamond for single-photon emission—overview and critical remarks. *New J. Phys.* **13**, 035024 (2011).
28. J. Riedrich-Moller, S. Pezzagna, J. Meijer, C. Pauly, F. Mucklich, M. Markham, A. M. Edmonds, C. Becher, Nanoimplantation and Purcell enhancement of single nitrogen-vacancy centers in photonic crystal cavities in diamond. *Appl. Phys. Lett.* **106**, 221103 (2015).
29. J. Meijer, B. Burchard, M. Domhan, C. Wittmann, T. Gaebel, I. Popa, F. Jelezko, J. Wrachtrup, Generation of single color centers by focused nitrogen implantation. *Appl. Phys. Lett.* **87**, 261909 (2005).
30. M. Lesik, P. Spinicelli, S. Pezzagna, P. Happel, V. Jacques, O. Salord, B. Rasser, A. Delobbe, P. Sudraud, A. Tallaire, J. Meijer, J. F. Roch, Maskless and targeted creation of arrays of colour centres in diamond using focused ion beam technology. *Phys. Status Solidi A* **210**, 2055–2059 (2013).
31. J. Riedrich-Moller, C. Arend, C. Pauly, F. Mucklich, M. Fischer, S. Gsell, M. Schreck, C. Becher, Deterministic coupling of a single silicon-vacancy color center to a photonic crystal cavity in diamond. *Nano Lett.* **14**, 5281–5287 (2014).
32. S. Tamura, G. Koike, A. Komatsubara, T. Teraji, S. Onoda, L. P. McGuinness, L. Rogers, B. Naydenov, E. Wu, L. Yan, F. Jelezko, T. Ohshima, J. Isoya, T. Shinada, T. Tanii, Array of bright silicon-vacancy centers in diamond fabricated by low-energy focused ion beam implantation. *Appl. Phys. Express* **7**, 115201 (2014).
33. T. Schroder, M. E. Trusheim, M. Walsh, L. Li, J. Zheng, M. Schukraft, A. Sipahigil, R. E. Evans, D. D. Sukachev, C. T. Nguyen, J. L. Pacheco, R. M. Camacho, E. S. Bielejec, M. D. Lukin, D. Englund, Scalable focused ion beam creation of nearly lifetime-limited single quantum emitters in diamond nanostructures. *Nat. Commun.* **8**, 15376 (2017).
34. J. Wang, X. Zhang, Y. Zhou, K. Li, Z. Wang, P. Peddibhoda, F. Liu, S. Bauerdick, A. Rudzinski, Z. Liu, W. Gao, Scalable fabrication of single silicon vacancy defect arrays in silicon carbide using focused ion beam. *Acs Photonics* **4**, 1054–1059 (2017).
35. L. Sapienza, M. Davanco, A. Badolato, K. Srinivasan, Nanoscale optical positioning of single quantum dots for bright and pure single-photon emission. *Nat. Commun.* **6**, 7833 (2015).
36. T. Schroder, M. Walsh, J. Zheng, S. Mouradian, L. Li, G. Malladi, H. Bakhru, M. Lu, A. Stein, M. Heuck, D. Englund, Scalable fabrication of coupled NV center–photonic crystal cavity systems by self-aligned N ion implantation. *Opt. Mater. Exp.* **7**, 1514–1524 (2017).
37. M. Schukraft, J. Zheng, T. Schroder, S. L. Mouradian, M. Walsh, M. E. Trusheim, H. Bakhru, D. R. Englund, Invited article: Precision nanoimplantation of nitrogen vacancy centers into diamond photonic crystal cavities and waveguides. *Apl Photonics* **1**, 020801 (2016).
38. L. Li, I. Bayn, M. Lu, C. Y. Nam, T. Schroder, A. Stein, N. C. Harris, D. Englund, Nanofabrication on unconventional substrates using transferred hard masks. *Sci. Rep.* **5**, 7802 (2015).
39. E. Neu, P. Appel, M. Ganzhorn, J. Miguel-Sanchez, M. Lesik, V. Mille, V. Jacques, A. Tallaire, J. Achard, P. Maletinsky, Photonic nano-structures on (111)-oriented diamond. *Appl. Phys. Lett.* **104**, 153108 (2014).
40. F. Shi, F. Kong, P. Zhao, X. Zhang, M. Chen, S. Chen, Q. Zhang, M. Wang, X. Ye, Z. Wang, Z. Qin, X. Rong, J. Su, P. Wang, P. Z. Qin, J. Du, Single-DNA electron spin resonance spectroscopy in aqueous solutions. *Nat. Methods* **15**, 697–699 (2018).
41. P. Maletinsky, S. Hong, M. S. Grinolds, B. Hausmann, M. D. Lukin, R. L. Walsworth, M. Loncar, A. Yacoby, A robust scanning diamond sensor for nanoscale imaging with single nitrogen-vacancy centres. *Nat. Nanotechnol.* **7**, 320–324 (2012).
42. M. S. Grinolds, S. Hong, P. Maletinsky, L. Luan, M. D. Lukin, R. L. Walsworth, A. Yacoby, Nanoscale magnetic imaging of a single electron spin under ambient conditions. *Nat. Phys.* **9**, 215–219 (2013).
43. I. Gross, W. Akhtar, V. Garcia, L. J. Martinez, S. Chouaieb, K. Garcia, C. Carretero, A. Barthelemy, P. Appel, P. Maletinsky, J. V. Kim, J. Y. Chauleau, N. Jaouen, M. Viret, M. Bibes, S. Fusil, V. Jacques, Real-space imaging of non-collinear antiferromagnetic order with a single-spin magnetometer. *Nature* **549**, 252–256 (2017).
44. L. Thiel, Z. Wang, M. A. Tschudin, D. Rohner, I. Gutierrez-Lezama, N. Ubrig, M. Gibertini, E. Giannini, A. F. Morpurgo, P. Maletinsky, Probing magnetism in 2D materials at the nanoscale with single-spin microscopy. *Science* **364**, 973–976 (2019).
45. P. Wang, S. Chen, M. Guo, S. Peng, M. Wang, M. Chen, W. Ma, R. Zhang, J. Su, X. Rong, F. Shi, T. Xu, J. Du, Nanoscale magnetic imaging of ferritins in a single cell. *Sci. Adv.* **5**, eaau8038 (2019).
46. L. Thiel, D. Rohner, M. Ganzhorn, P. Appel, E. Neu, B. Müller, R. Kleiner, D. Koelle, P. Maletinsky, Quantitative nanoscale vortex imaging using a cryogenic quantum magnetometer. *Nat. Nanotechnol.* **11**, 677–681 (2016).
47. J. F. Ziegler, M. D. Ziegler, J. P. Biersack, SRIM–The stopping and range of ions in matter (2010). *Nucl. Instrum. Methods B* **268**, 1818–1823 (2010).
48. B. J. M. Hausmann, M. Khan, Y. N. Zhang, T. M. Babinec, K. Martinick, M. McCutcheon, P. R. Hemmer, M. Loncar, Fabrication of diamond nanowires for quantum information processing applications. *Diamond Relat. Mater.* **19**, 621–629 (2010).
49. N. Hedrich, D. Rohner, M. Batzer, P. Maletinsky, B. J. Shields, Parabolic diamond scanning probes for single-spin magnetic field imaging. *Phys. Rev. Appl.* **14**, 064007 (2020).
50. M. J. Burek, Y. Chu, M. S. Liddy, P. Patel, J. Rochman, S. Meesala, W. Hong, Q. Quan, M. D. Lukin, M. Loncar, High quality-factor optical nanocavities in bulk single-crystal diamond. *Nat. Commun.* **5**, 5718 (2014).
51. M. S. Grinolds, P. Maletinsky, S. Hong, M. D. Lukin, R. L. Walsworth, A. Yacoby, Quantum control of proximal spins using nanoscale magnetic resonance imaging. *Nat. Phys.* **7**, 687–692 (2011).
52. J. F. Barry, J. M. Schloss, E. Bauch, M. J. Turner, C. A. Hart, L. M. Pham, R. L. Walsworth, Sensitivity optimization for NV-diamond magnetometry. *Rev. Mod. Phys.* **92**, 015004 (2020).
53. S. Sangtawesin, B. L. Dwyer, S. Srinivasan, J. J. Allred, L. V. H. Rodgers, K. De Greve, A. Stacey, N. Dontschuk, K. M. O'Donnell, D. Hu, D. A. Evans, C. Jaye, D. A. Fischer, M. L. Markham, D. J. Twitchen, H. Park, M. D. Lukin, N. P. de Leon, Origins of diamond surface noise probed by correlating single-spin measurements with surface spectroscopy. *Phys. Rev. X* **9**, 031052 (2019).
54. N. Bar-Gill, L. M. Pham, A. Jarmola, D. Budker, R. L. Walsworth, Solid-state electronic spin coherence time approaching one second. *Nat. Commun.* **4**, 1743 (2013).
55. B. A. Myers, A. Ariyaratne, A. C. B. Jayich, Double-quantum spin-relaxation limits to coherence of near-surface nitrogen-vacancy centers. *Phys. Rev. Lett.* **118**, 197201 (2017).
56. Y. F. Chen, Nanofabrication by electron beam lithography and its applications: A review. *Microelectron. Eng.* **135**, 57–72 (2015).
57. S. Mouradian, N. H. Wan, T. Schroder, D. Englund, Rectangular photonic crystal nanobeam cavities in bulk diamond. *Appl. Phys. Lett.* **111**, 021103 (2017).
58. N. H. Wan, S. Mouradian, D. Englund, Two-dimensional photonic crystal slab nanocavities on bulk single-crystal diamond. *Appl. Phys. Lett.* **112**, 141102 (2018).
59. C. Chia, B. Machielse, A. Shams-Ansari, M. Loncar, Development of hard masks for reactive ion beam angled etching of diamond. *Opt. Express* **30**, 14189–14201 (2022).
60. B. Naydenov, F. Reinhard, A. Lammle, V. Richter, R. Kalish, U. F. S. D'Haenens-Johansson, M. Newton, F. Jelezko, J. Wrachtrup, Increasing the coherence time of single electron spins in diamond by high temperature annealing. *Appl. Phys. Lett.* **97**, 242511 (2010).
61. Y. Chu, N. P. de Leon, B. J. Shields, B. Hausmann, R. Evans, E. Togan, M. J. Burek, M. Markham, A. Stacey, A. S. Zibrov, A. Yacoby, D. J. Twitchen, M. Loncar, H. Park, P. Maletinsky, M. D. Lukin, Coherent optical transitions in implanted nitrogen vacancy centers. *Nano Lett.* **14**, 1982–1986 (2014).
62. F. Favaro de Oliveira, D. Antonov, Y. Wang, P. Neumann, S. A. Momenzadeh, T. Haussermann, A. Pasquarelli, A. Denisenko, J. Wrachtrup, Tailoring spin defects in diamond by lattice charging. *Nat. Commun.* **8**, 15409 (2017).
63. E. D. Herbschleb, H. Kato, Y. Maruyama, T. Danjo, T. Makino, S. Yamasaki, I. Ohki, K. Hayashi, H. Morishita, M. Fujiwara, N. Mizuochi, Ultra-long coherence times amongst room-temperature solid-state spins. *Nat. Commun.* **10**, 3766 (2019).
64. T. Luhmann, R. John, R. Wunderlich, J. Meijer, S. Pezzagna, Coulomb-driven single defect engineering for scalable qubits and spin sensors in diamond. *Nat. Commun.* **10**, 4956 (2019).
65. A. Watanabe, T. Nishikawa, H. Kato, M. Fujie, M. Fujiwara, T. Makino, S. Yamasaki, E. D. Herbschleb, N. Mizuochi, Shallow NV centers augmented by exploiting n-type diamond. *Carbon* **178**, 294–300 (2021).

66. R. J. Epstein, F. M. Mendoza, Y. K. Kato, D. D. Awschalom, Anisotropic interactions of a single spin and dark-spin spectroscopy in diamond. *Nat. Phys.* **1**, 94–98 (2005).

**Acknowledgments:** The fabrication of diamond device was performed at the USTC Center for Micro and Nanoscale Research and Fabrication, and we thank W. Liu, Y. Wei, X. W. Wang, C. L. Xin, and H. F. Zuo for their assistance in EBL, deposition, and etching process. We thank B. Cui for helpful discussion of the PMGI etching. **Funding:** This work was supported by the National Key R&D Program of China (grants no. 2021YFB3202800), the CAS (grants no. XDC07000000, GJJSTD20200001, and QYZDYSSW-SLH004), the National Natural Science Foundation of China (grants no. 81788101, 11775209, 12104447, 11804329, and T2125011), the Innovation Program for Quantum Science and Technology (grant no. 2021ZD0302200), the Anhui Initiative in Quantum Information Technologies (grant no. AHY050000), the China Postdoctoral Science Foundation (grant no. 2020 M671858), the Fundamental Research Funds for the Central Universities, and the USTC Research Funds of the Double First-Class Initiative. **Author contributions:** J.D. and Y.W. proposed the idea and supervised the experiment. M.W. designed the fabrication process. M.W., X.Y., P.Y., H.S., H.L., and J.Z. performed the fabrication process. M.W. and H.S. collected and analyzed the experiment data. M.W., P.Y., P.W., and F.S. constructed the experimental setup. Y.W., M.W., and J.D. wrote the paper. All authors discussed the results and commented on the manuscript. **Competing interests:** The authors declare that they have no competing interests. **Data and materials availability:** All data needed to evaluate the conclusions in the paper are present in the paper and/or the Supplementary Materials.

Submitted 5 January 2022
Accepted 10 August 2022
Published 23 September 2022
10.1126/sciadv.abn9573